

Light-Emission and Excited-State Dynamics in Tm^{2+} Doped CsCaCl_3 , CsCaBr_3 , and CsCaI_3

Judith Grimm, J. Freek Suyver,[†] Eva Beurer, Graham Carver, and Hans U. Güdel*

Department of Chemistry and Biochemistry, University of Bern, Freiestrasse 3, 3012 Bern, Switzerland

Received: October 17, 2005; In Final Form: November 23, 2005

The light-emission and photophysical properties of $\text{CsCaCl}_3\text{:Tm}^{2+}$ (1.04%), $\text{CsCaBr}_3\text{:Tm}^{2+}$ (0.48%), and $\text{CsCaI}_3\text{:Tm}^{2+}$ (0.76%) are presented. We find that Tm^{2+} is a multiple emitter under 21 834 cm^{-1} laser excitation at low temperatures in all three compounds. Several distinct types of emission are observed and characterized: sharp and long-lived 4f–4f emission in the infrared (IR) and up to four broad and fast decaying emission bands in the near-IR and visible, originating from the 4f–5d states of Tm^{2+} . The optical spectroscopic properties of the samples are compared, and we find that the measured differences in the relative intensities and the shifts in the position of the emissions can be related to the chemical influence on the absorption and emission properties of Tm^{2+} . Thus, it nicely illustrates the principle of chemical variation on the optical spectroscopic properties. An investigation of the temperature dependence of the luminescence yields important information about the dynamics of the excited states. The interplay and competition between radiative and nonradiative pathways is explained and modeled using a single configurational coordinate approach.

1. Introduction

The most common valence state of lanthanides in solids is the trivalent one. The basic features of the optical spectra of trivalent lanthanide ions in solids are well understood, and an enormous amount of studies describing the light-emission properties can be found in the literature. Some rare earth ions may also occur in the divalent state. Eu^{2+} , Yb^{2+} , and Sm^{2+} have received most attention among them.¹ These are the lanthanides that are most easily stabilized in their divalent oxidation state. In some lattices, Tm^{2+} can also be stabilized in its divalent state, but most Tm^{2+} compounds are air sensitive,² and they have received considerably less attention in the past.

Several aspects of the optical spectroscopic properties of Tm^{2+} in alkaline earth fluorides have been described and interpreted already in the 1960s by McClure, Kiss, and Loh.^{3–5} An early research highlight was the demonstration of laser oscillation on the intraconfigurational $^2\text{F}_{5/2} \rightarrow ^2\text{F}_{7/2}$ transition in $\text{CaF}_2\text{:Tm}^{2+}$ at low temperatures at the dawn of the invention of optical lasers.⁶ It has also been known for decades that, in addition to the $^2\text{F}_{5/2} \rightarrow ^2\text{F}_{7/2}$ emission, the lowest 4f–5d state is spontaneously emitting.⁷ Due to this, Tm^{2+} has been suggested for application in IR counting devices as early as 1966.⁷ Spontaneous 5d–4f emission from the lowest 4f–5d excited state was since reported for Tm^{2+} doped SrB_4O_7 ,⁸ SrCl_2 ,⁹ BaZnCl_4 , SrZnCl_4 ,¹⁰ and CsCaBr_3 ,¹¹ whereas this emission was not reported for Tm^{2+} in alkaline earth fluorides.¹² Recently, we described the light-emission properties of Tm^{2+} in CsCaBr_3 , where we have the most unusual situation of five different types of spontaneous emission processes.¹¹ In particular, emission from higher lying 5d–4f states in Tm^{2+} was observed and characterized.

The 4f–5d states are affected by changes in the ligand field, whereas a change in the host lattice will have only a small effect

on the 4f–4f excited states as these are essentially ligand-field independent. This prompted us to extend our studies of Tm^{2+} doped compounds. In the present contribution, we give a detailed account of the light-emission properties of the Tm^{2+} doped cubic perovskites CsCaBr_3 and CsCaCl_3 . For a comparative discussion of the excited-state dynamics, we include the results of the isostructural $\text{CsCaI}_3\text{:Tm}^{2+}$. An account of the spectroscopic properties of $\text{CsCaI}_3\text{:Tm}^{2+}$ together with $\text{RbCaI}_3\text{:Tm}^{2+}$ will be provided separately.¹³ The chemical variation along the perovskite series CsCaCl_3 , CsCaBr_3 , and CsCaI_3 leads to a systematic variation of the light-emission properties. These can be understood from the competition between radiative and nonradiative relaxation processes in the photophysics of Tm^{2+} . In section 4.4, we provide a simple model based on rate equations, which nicely reproduces the observed trends.

2. Experimental Section

2.1. Synthesis and Crystal Growth. Single crystals of CsCaCl_3 , CsCaBr_3 , and CsCaI_3 doped with Tm^{2+} were grown by the Bridgman technique. For the synthesis, stoichiometric amounts of CsX ($\text{X} = \text{Cl}, \text{Br}, \text{I}$) and CaX_2 were mixed and Tm^{2+} was prepared in situ by synproportionation of TmX_3 (prepared via the ammonium halide route¹⁴ from 99.999% pure Tm_2O_3 from Johnson Matthey) and Tm metal (Alfa Aesar 99.9%). All starting materials are hygroscopic and were handled in a glovebox under N_2 atmosphere. Dark green crystals of good optical quality with diameters up to 2 mm \times 2 mm \times 2 mm were obtained. The crystals were checked for purity by X-ray powder diffraction. The absolute concentrations of Tm in the crystals were determined with ICP-OES and are 1.04%, 0.48%, and 0.76% in CsCaCl_3 , CsCaBr_3 , and CsCaI_3 , respectively. The use of tantalum rather than the more commonly used silica ampules was found to be indispensable for obtaining crystals that contained no Tm^{3+} . Crystals grown from silica ampules contain trace amounts of Tm^{3+} because under such crystal growth conditions Tm^{2+} is easily oxidized by silica. Due to the hygroscopic nature of the crystals, the handling occurred under inert atmosphere at all times. For absorption measurements, the

* To whom correspondence should be addressed. E-mail: hans-ulrich.guedel@iac.unibe.ch. Tel: +41 31 631 42 49. Fax: +41 31 631 43 99.

[†] Present address: Philips Research, High Tech campus 34, 5656 AE Eindhoven, The Netherlands.

samples were polished in a drybox and enclosed in an airtight copper cell equipped with a quartz window. Thermal contact of the crystal with the sample holder was provided through the application of copper grease (Lake Shore Cryotronics Inc.). For luminescence measurements, the samples were sealed into quartz ampules under partial pressure of He, which serves as an inert atmosphere as well as a heat transmitter.

2.2. Spectroscopic Measurements. Sample cooling was achieved with a closed-cycle cryostat (Air Products) for absorption and with the He gas flow technique for emission measurements. Absorption spectra were recorded on a Cary 6000i spectrometer (Varian). Emission spectra were excited with the 457.9 nm (21 834 cm^{-1}) line of an Ar^+ laser (Spectra Physics 2060-10 SA). The sample luminescence was dispersed either with a 0.85 m double monochromator (Spex 1402) or a 0.75 m single monochromator (Spex 1702). A PMT (Hamamatsu P3310-01) and a photon counting system (Stanford Research 400) or a Ge detector (ADC 403L and 403HS) interfaced to a lock-in amplifier (Stanford Research 830) were used for detection of the signal in the visible and IR ranges, respectively. The luminescence transients were measured with either the Ar^+ laser and an acousto-optic modulator (Coherent 305, Stanford Research DS 345 function generator) or the fundamental (1064 nm = 9398 cm^{-1}) or the third harmonic (355 nm = 28 169 cm^{-1}) of a pulsed Nd:YAG laser (Quanta Ray DCR 3, 20 Hz). Transient signals were detected as described above using a multichannel scaler (Stanford Research 430) or an oscilloscope (Tektronix TDS 540a). All luminescence spectra were corrected for the sensitivity of the detection system and are displayed as photon counts vs energy.

3. Results

Parts a and b of Figure 1 show the 10 K emission spectra of $\text{CsCaCl}_3\text{:Tm}^{2+}$ and $\text{CsCaBr}_3\text{:Tm}^{2+}$ along with the corresponding absorption spectra 1c and 1d, respectively. Laser excitation for the emission spectra occurred at 21 834 cm^{-1} for both samples. The observed emission bands are labeled A–E, and the electronic transitions to which they refer will be discussed in section 4. The same notation is used for both samples. The band positions and the partition of the emitted photons at 10 K among the five bands A–E are given in Table 1 including the results of $\text{CsCaI}_3\text{:Tm}^{2+}$. The positions of the broad emission bands B–E all undergo a redshift of about 300–350 cm^{-1} , as the host lattice is changed from the chloride to the bromide and about 900 cm^{-1} from the bromide to the iodide. The sharp emission A, in contrast, is shifted to lower energy by only about 15 cm^{-1} from chloride to bromide and about 11 cm^{-1} from bromide to iodide. The partition of photons among the bands at 10 K is very different for the three samples. While D is absolutely dominant in the bromide and iodide, both B and D have sizable intensity in the chloride. All the transitions A–E are observable at 10 K in the bromide and iodide, whereas C could not be detected in the chloride.

Parts a and b of Figure 2 show the high-resolution 10 K emission spectra of bandsystem A in $\text{CsCaCl}_3\text{:Tm}^{2+}$ and $\text{CsCaBr}_3\text{:Tm}^{2+}$, along with the corresponding 10 K absorption spectra 2c and 2d, respectively. Laser excitation for the emission spectra occurred at 21 834 cm^{-1} for both samples. Disregarding the lines marked with an asterisk, which we assign to nonregular crystal sites, the sharp-line spectra of the chloride and bromide resemble each other and will be analyzed in section 4.3.

In Figure 3, the emission spectra of $\text{CsCaCl}_3\text{:Tm}^{2+}$ and $\text{CsCaBr}_3\text{:Tm}^{2+}$, respectively, are shown at three different temperatures, 10, 130, and 300 K. The spectra are scaled within

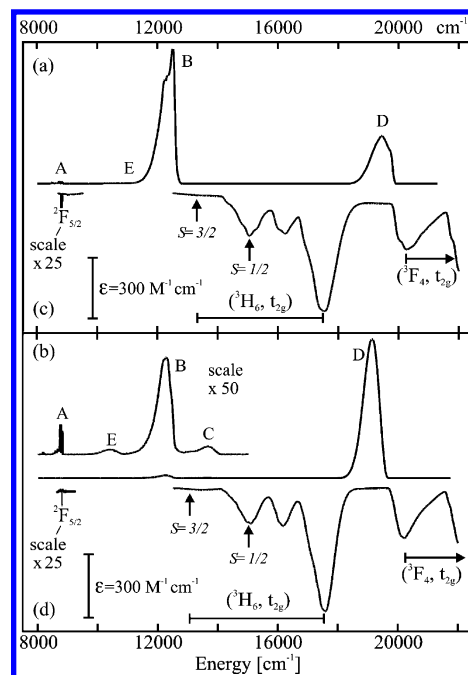


Figure 1. Survey emission (a) and onset of single-crystal absorption spectrum (c) of $\text{CsCaCl}_3\text{:1.04% Tm}^{2+}$ recorded at 10 K. In (b) and (d), the analogous data are presented for $\text{CsCaBr}_3\text{:0.48% Tm}^{2+}$. Both emissions were photoexcited at 21 834 cm^{-1} . Note the scale changes in (b), (c), and (d). The labels of the emission bands are used in the text. The range of ($^3\text{H}_6$, t_{2g}) and the onset of ($^3\text{F}_4$, t_{2g}) absorptions are indicated. The first $S = 3/2$ and $S = 1/2$ absorption bands within the ($^3\text{H}_6$, t_{2g}) multiplet are marked by arrows.

TABLE 1: Positions in cm^{-1} of Emission Bands A–E at 10 K and Integrated Photon Counts as a Percentage of the Total Photon Flux at 10 K in Tm^{2+} Doped CsCaCl_3 , CsCaBr_3 , and CsCaI_3 . Laser excitation occurred at 21 834 cm^{-1}

compound	emission	position (cm^{-1})	integrated photon counts (%)
CsCaCl_3	D	19 450	36.5
	B	12 497	63
	E	10 647	0.2
	A	8810	0.3
CsCaBr_3	D	19 152	97.6
	C	13 676	0.2
	B	12 237	2
	E	10 370	0.1
CsCaI_3	A	8796	0.1
	D	18 344	92.7
	C	12 703	2.3
	B	11 348	4.6
	E	9503	0.1
	A	8785	0.3

3a and 3b, therefore intensities at different temperatures can be compared. There is a general shift of photons from high-energy to low-energy bands in both samples as the temperature is raised. The temperature dependence of the integrated photon counts of the three dominant emissions A, B (+ C in $\text{CsCaI}_3\text{:Tm}^{2+}$), and D under 21 834 cm^{-1} excitation is shown in Figure 4 for $\text{CsCaCl}_3\text{:Tm}^{2+}$, $\text{CsCaBr}_3\text{:Tm}^{2+}$, and $\text{CsCaI}_3\text{:Tm}^{2+}$, respectively. The data will be analyzed in section 4.4. In Figure 5, the temperature dependences of the integrated photon counts and the lifetime of emission B in $\text{CsCaCl}_3\text{:Tm}^{2+}$ (5a) and $\text{CsCaBr}_3\text{:Tm}^{2+}$ (5b) are compared. For both compounds, the lifetime is constant below 100 K, whereas the intensity shows an increase with increasing temperature. Above 100 K in the chloride and 150 K in the bromide, the lifetime decreases along with the integrated photon counts. The lifetimes of the emission bands

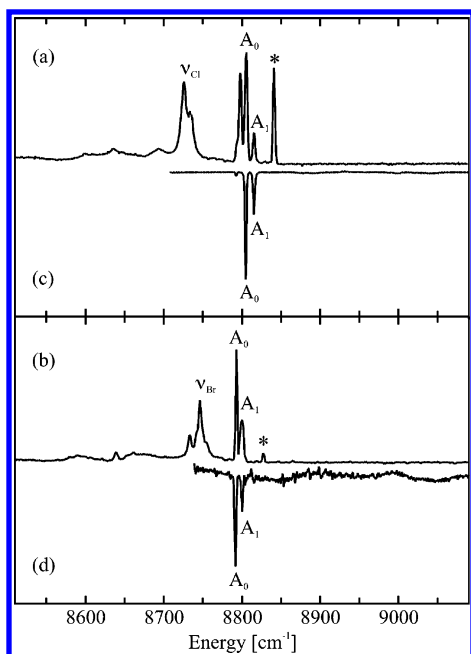


Figure 2. The 10 K emission spectrum of the $^2F_{5/2} \rightarrow ^2F_{7/2}$ transition (band A) of Tm^{2+} is shown in (a) for CsCaCl_3 and (b) for CsCaBr_3 . Both emissions were photoexcited at $21\,834\text{ cm}^{-1}$. The 10 K single-crystal absorption spectrum of the $^2F_{7/2} \rightarrow ^2F_{5/2}$ transition of Tm^{2+} is shown in (c) for CsCaCl_3 and (d) for CsCaBr_3 . The emission lines that are labeled with an asterisk are attributed to Tm^{2+} on nonregular sites (see text). The bands labeled ν_{Cl} and ν_{Br} are vibronic sidebands of the $^2F_{5/2} \rightarrow ^2F_{7/2}$ transition in $\text{CsCaCl}_3:\text{Tm}^{2+}$ and $\text{CsCaBr}_3:\text{Tm}^{2+}$, respectively.

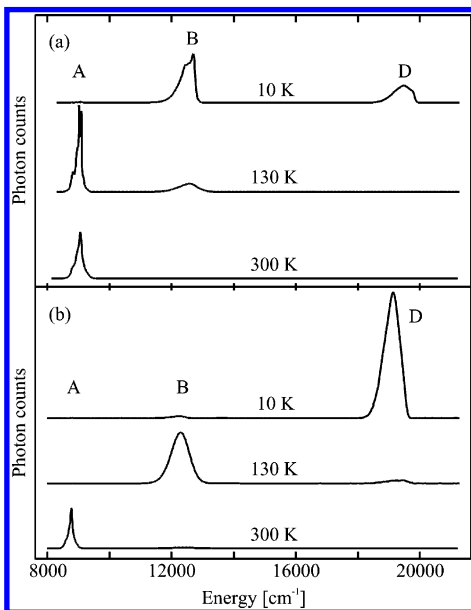


Figure 3. Emission spectra of Tm^{2+} in (a) CsCaCl_3 and (b) CsCaBr_3 at three temperatures: 10, 130, and 300 K. The emission was photoexcited at $21\,834\text{ cm}^{-1}$. The spectra are shifted arbitrarily along the vertical axis. The spectra within (a) or (b) have the same scale, therefore intensities at different temperatures can be compared. Only the prominent emissions A, B, and D are labeled.

A, B, and D of Tm^{2+} are given in Table 2 for CsCaCl_3 , CsCaBr_3 , and CsCaI_3 . They will be used to determine the decay rate constants in the rate equation modeling in section 4.4.

4. Analysis

4.1. Structures and Sites. CsCaCl_3 and CsCaBr_3 are cubic perovskites at room temperature, crystallizing in the space group

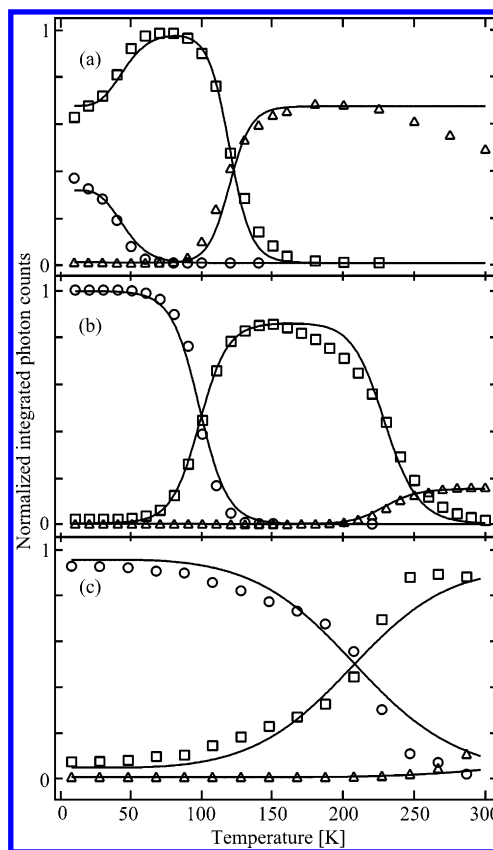


Figure 4. Temperature dependence of the integrated photon counts (normalized to 1 for the most intense band) of the three dominant emissions: Δ , A; \square , B (+C in $\text{CsCaI}_3:\text{Tm}^{2+}$); and \circ , D in (a) $\text{CsCaCl}_3:\text{Tm}^{2+}$, (b) $\text{CsCaBr}_3:\text{Tm}^{2+}$, and (c) $\text{CsCaI}_3:\text{Tm}^{2+}$. The photon counts were corrected for the decreasing absorption cross section with increasing temperature at the excitation energy of $21\,834\text{ cm}^{-1}$. The solid lines represent simulations of the data using the model in section 4.4 (eq 2). The input and fit parameters are listed in Tables 3 and 4, respectively.

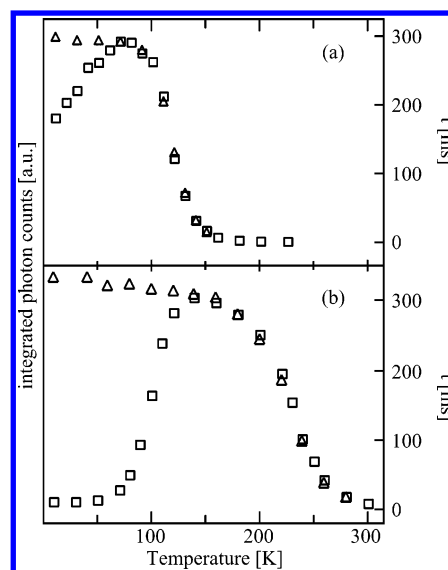


Figure 5. Temperature dependence of emission lifetimes (Δ) and intensities (\square) of band B in (a) $\text{CsCaCl}_3:\text{Tm}^{2+}$ and (b) in $\text{CsCaBr}_3:\text{Tm}^{2+}$.

$Pm\bar{3}m$.^{15,16} The Tm^{2+} ions replace Ca^{2+} on site 1(b) with O_h point symmetry. Both samples undergo phase transitions upon cooling, which is common for cubic perovskites. The cubic to tetragonal phase change at $T = 95\text{ K}$ in CsCaCl_3 is well documented in the literature.^{17,18} The site symmetry of Ca^{2+}

TABLE 2: Measured Lifetimes τ of the Emission Bands D, B, and A of Tm^{2+} Doped CsCaCl_3 , CsCaBr_3 , and CsCaI_3

emission	T		CsCaCl_3	CsCaBr_3	CsCaI_3
D^a	10 K	τ	904 ns	1.7 μs	1 μs
		τ_{calc}	1.5 μs	1.8 μs	2 μs
B	10 K	τ	296 μs	323 μs	391 μs
A	300 K	τ	501 μs	534 μs	650 μs

^a The radiative lifetime τ_{calc} of emission D is calculated from eq 7 (see section 4.4).

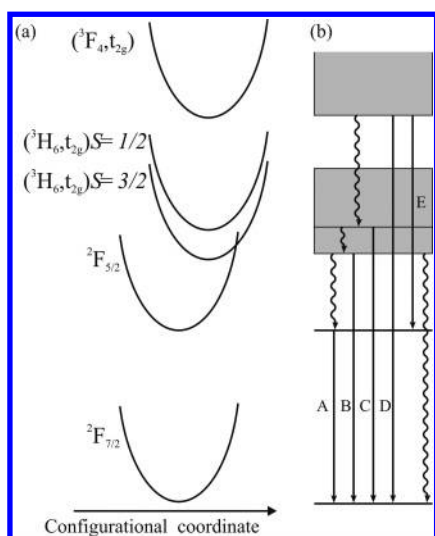


Figure 6. (a) Schematic single configurational coordinate (SCC) diagram of Tm^{2+} assuming harmonic potentials and equal force constants for all states. The emitting excited states are schematically displayed in (b) with the radiative and nonradiative processes indicated as straight and curly arrows, respectively. The labeling of the transitions corresponds to Figure 1 and Tables 1 and 2.

below the phase change is C_{4h} .¹⁷ The distortion from O_h symmetry at the Ca^{2+} site is small.¹⁸ CsCaBr_3 undergoes two phase changes at 237 and 145 K, respectively.¹⁶ CsCaI_3 crystallizes in the orthorhombic $Pnma$ phase at 300 K.¹⁹ The Ca^{2+} in the orthorhombic $Pnma$ phase has site symmetry C_i . Regardless of the phase changes, the Tm^{2+} ion is always coordinated by six X^- ($X^- = \text{Cl}, \text{Br}, \text{I}$). From the spectroscopic data of the three samples, we conclude that only band splitting due to symmetry reduction is observable in bandsystem A and is in the order of a few wavenumbers (vide infra). The data interpretation of the 4f–5d states is therefore done in the octahedral approximation.

4.2. Emitting States and Spectral Assignments. The assignment of the emission bands has already been discussed for $\text{CsCaBr}_3\text{:Tm}^{2+}$ in ref 11. Figure 6a shows a schematic single configurational coordinate (SCC) diagram of the lowest excited states of Tm^{2+} assuming harmonic potentials and equal force constants for all states. The relevant radiative and nonradiative relaxation processes are indicated in Figure 6b as straight and curly arrows, respectively.

Tm^{2+} has a $(4f)^{13}$ ground-state electron configuration, that is, it is isoelectronic with Yb^{3+} . The two multiplets arising from the $(4f)^{13}$ electron configuration are $^2F_{7/2}$ and $^2F_{5/2}$. The energy of the $^2F_{5/2}$ multiplet is about 1200 cm^{-1} lower in Tm^{2+} than in Yb^{3+} , reflecting the smaller spin–orbit coupling in Tm^{2+} .²⁰ As seen in Figure 2, the sharp 4f–4f bands are observed in absorption and emission around 8800 cm^{-1} in both $\text{CsCaCl}_3\text{:Tm}^{2+}$ and $\text{CsCaBr}_3\text{:Tm}^{2+}$ at 10 K. The fine structure will be analyzed in section 4.3. For the modeling in section 4.4, the total 4f–4f emission intensity (transition A in Figure 6) will be considered.

In the absorption spectra in parts c and d of Figure 1, all the bands above 10 000 cm^{-1} are due to 4f–5d transitions, in which one electron is promoted from the 4f orbitals to the 5d orbitals. These absorption transitions are between 1 and 4 orders of magnitude more intense than the intraconfigurational 4f–4f transitions. In contrast to the latter, the 4f–5d transitions are parity allowed, which can result in a huge increase in the oscillator strength. The states resulting from the $(4f)^{12}(5d)^1$ electron configuration are represented with a displacement along the configurational coordinate in Figure 6, in agreement with the observed broad absorption and emission bands. The displacement results from the different chemical bonding in the $(4f)^{13}$ and $(4f)^{12}(5d)^1$ configurations. The $(4f)^{12}(5d)^1$ electron configuration has a total degeneracy of 910, and energy splittings occur as a result of various interactions.

An important interaction in the $(4f)^{12}(5d)^1$ configuration is the ligand field interaction of the 5d electron. The octahedral ligand field splits the 5d orbitals into t_{2g} and e_g sets, separated by 10 Dq. All bands below 25 000 cm^{-1} that are shown in the absorption spectra (parts a and b of Figure 1) can be attributed to excited states with the 5d electron in the t_{2g} set. The $(4f)^{12}$ part of the configuration is split into the $^{2S+1}L_J$ terms of Tm^{3+} by the Coulombic repulsion and the spin–orbit coupling of the 4f electrons. Thus, the energy multiplets of the Tm^{2+} $(4f)^{12}(5d)^1$ configuration can be roughly characterized as $(^{2S+1}L_J, t_{2g})$ and $(^{2S+1}L_J, e_g)$. For Tm^{2+} , we expect each of these multiplets to be split into a set of lower energy high-spin $S = 3/2$ and a set of higher energy low-spin $S = 1/2$ states due to the isotropic exchange part of the Coulombic interaction between the 4f and 5d electrons.¹¹ As a consequence, the lowest-energy $(4f)^{12}(5d)^1$ bands are expected to have formally “spin-forbidden” character, which will manifest itself in weaker oscillator strengths compared to the formally “spin-allowed” bands.³

The emission band B (Figures 1 and 6) originates from the lowest-energy 4f–5d state. The corresponding weak absorption band is shown in Figure 1c for $\text{CsCaCl}_3\text{:Tm}^{2+}$ and 1d for $\text{CsCaBr}_3\text{:Tm}^{2+}$. Band B is thus assigned as a “spin-forbidden” 5d–4f transition from $(^3H_6, t_{2g}) S = 3/2$ to $^2F_{7/2}$. Band C is correlated with the first intense 4f–5d absorption band and is therefore assigned as a “spin-allowed” 5d–4f transition from $(^3H_6, t_{2g}) S = 1/2$ to $^2F_{7/2}$. Quite to our surprise, we observed emission from an even higher lying 4f–5d state: band D is assigned to a transition from the lowest excited state of the $(^3F_4, t_{2g})$ multiplet to the $^2F_{7/2}$ groundstate. Finally, band E is the interexcited-state transition from $(^3F_4, t_{2g})$ to $^2F_{5/2}$. The spin of the emitting $(^3F_4, t_{2g})$ state cannot be specified. Apparently, spin is not as well defined in the $(^3F_4, t_{2g})$ multiplet as it is in $(^3H_6, t_{2g})$.^{11,21}

4.3. 4f–4f Emission A and Crystal Field Splitting of the $^2F_{5/2}$ and $^2F_{7/2}$. The high-resolution absorption and emission data obtained at 10 K in the region of the 4f–4f transitions (Figure 2) exhibit considerable fine structure. Some lines around 8800 cm^{-1} in both compounds coincide in absorption and emission. They are labeled A_0 and A_1 , and they can be assigned to electronic origins as shown in the diagram of Figure 7. Since the intensity ratio of A_1 and A_0 was found to increase with temperature between 10 and 30 K, the splitting between A_0 and A_1 is necessarily an excited-state splitting. Figure 7 is a schematic representation of the splitting of $^2F_{7/2}$ and $^2F_{5/2}$ in an O_h (first step) and then C_{4h} or C_i (small distortion from O_h) crystal field. The octahedral splittings are of the order of several hundred cm^{-1} ,²² and an unambiguous assignment of absorption or emission features outside the 8800 cm^{-1} region to electronic origins is not possible. The situation is very similar to Yb^{3+} in

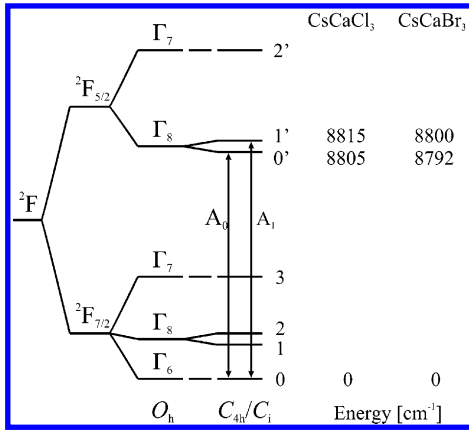


Figure 7. Schematic representation of the crystal field (CF) splitting of the $^2F_{7/2}$ and $^2F_{5/2}$ states of Tm²⁺ in CsCaCl₃ and CsCaBr₃. The energies of the CF levels are determined from Figure 2.

many host lattices. Unlike 4f–4f transitions in most other lanthanides, the $^2F_{7/2} \leftrightarrow ^2F_{5/2}$ bands in (4f)¹³ are characterized by the presence of strong vibronic sidebands. The bands labeled ν_{Cl} and ν_{Br} in the emission spectra of Figure 2 are such bands. Their identity as vibronic sidebands is confirmed by the reduced energy difference to the strong A_0 and A_1 origins in the bromide, a result of the smaller vibrational energies in the bromide. At the phase transitions of the host lattice, the site symmetry of Tm²⁺ is reduced from O_h to C_{4h} and C_i in the chloride and bromide, respectively. The degree of the distortion from O_h must be relatively small, however, since the splitting of $^2F_{5/2}$ (Γ_8) into the two Kramer's doublets $0'$ and $1'$ is only 10 and 8 cm⁻¹, respectively. The bands marked with asterisks in the emission spectra of Figure 2 are assigned to other species due to their different excitation spectrum. Tm²⁺ ions on some defect sites or Tm²⁺ pair transitions are possibilities.

4.4. Modeling the Excited-State Dynamics. The very pronounced redistribution of intensity with temperature among the three major emissions A, B, and D (Figures 3 and 4) provides clear evidence for thermally activated nonradiative relaxation processes. A simple model to treat such nonradiative processes is based on the single configurational coordinate (SCC) model.²³ The SCC diagram for Tm²⁺ doped halides is shown in Figure 6a where the configurational coordinate represents an effective accepting mode for the relaxation process. To model the temperature dependence of emissions A, B, and D, we simplified the SCC diagram. Since emission C is absent in CsCaCl₃ and very weak at all temperatures in the bromide, we left emission C out of the calculations. In the iodide, emission C is not negligible and therefore the integrated photon counts of emission B and C were added together in order to keep the model simple. Emission E shows the same temperature dependence as emission D, because the initial state is the same. The simplified SCC diagram that contains all the relevant radiative (straight arrows) and nonradiative processes (curly arrows) that are considered is shown in Figure 8. The state $|0\rangle$ corresponds to the $^2F_{7/2}$ ground state of Tm²⁺, $|1\rangle$ to $^2F_{5/2}$, $|2\rangle$ to $(^3H_6, t_{2g})S = 3/2$, and $|3\rangle$ to $(^3F_4, t_{2g})$. The radiative and nonradiative rate constants are labeled R_i and W_{ij} , respectively. Subscript i stands for the initial state and subscript j for the final state. The ratio of photons in the emission bands D and E is given by the branching ratios η_{30} and η_{31} , with $\eta_{30} + \eta_{31} = 1$. P is the laser power and σ the absorption cross section at the excitation energy.

For the laser powers used in our experiments, we can assume that the ground-state population N_0 is not affected by the excitation. We further assume that multiphonon relaxation from $|1\rangle$ to $|0\rangle$ is negligible. The following rate equations then

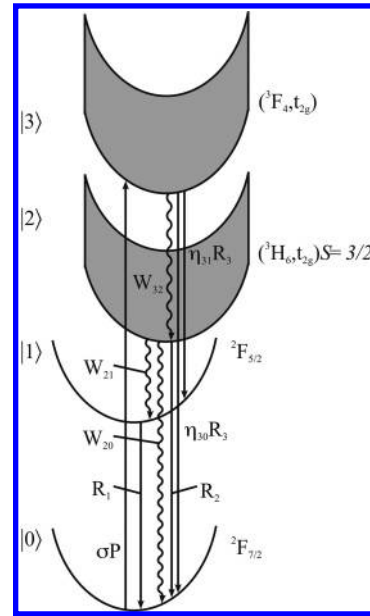


Figure 8. Simplified SCC diagram of Tm²⁺ to model the temperature dependence of the three major emissions A, B, and D. The four emissions in the SCC diagram correspond to the following transitions: A, $|1\rangle \rightarrow |0\rangle$; B, $|2\rangle \rightarrow |0\rangle$; D, $|3\rangle \rightarrow |0\rangle$; E, $|3\rangle \rightarrow |1\rangle$. Curly arrows are used to indicate nonradiative processes (W_{ij}) and straight arrows for radiative transitions (R_i). The branching ratios η_{30} and η_{31} determine the ratio of photons in the emission bands D and E, with $\eta_{30} + \eta_{31} = 1$. P is the laser power and σ the absorption cross section at the excitation energy.

describe the evolution of the excited-state populations N_i ($i = 1, \dots, 3$) upon excitation

$$\begin{aligned} \frac{dN_3}{dt} &= \sigma P N_0 - W_{32} N_3 - R_3 N_3 \\ \frac{dN_2}{dt} &= W_{32} N_3 - (W_{21} + W_{20} + R_2) N_2 \\ \frac{dN_1}{dt} &= W_{21} N_2 + \eta_{31} R_3 N_3 - R_1 N_1 \end{aligned} \quad (1)$$

The steady state solutions are

$$\begin{aligned} N_3 &= \frac{\sigma P N_0}{W_{32} + R_3} \\ N_2 &= \frac{\sigma P N_0 W_{32}}{(W_{21} + W_{20} + R_2)(W_{32} + R_3)} \\ N_1 &= \frac{\sigma P N_0 (\eta_{31} R_3 (W_{21} + W_{20} + R_2) + W_{32} W_{21})}{R_1 (W_{21} + W_{20} + R_2)(W_{32} + R_3)} \end{aligned} \quad (2)$$

The temperature dependence of the nonradiative decay rate constants W_{ij} is calculated within the framework of the SCC model.²⁴ We assume linear coupling and harmonic potentials. W_{ij} can be written as²⁵

$$W_{ij} = C_{ij} F_{ij} \quad (3)$$

where C_{ij} is the electronic factor and F_{ij} the thermal Franck–Condon factor.

The temperature-dependent Franck–Condon factor F_{ij} can be written as²⁵

$$F_{ij}(T) =$$

$$\exp(-S_{ij}(1 + 2m)) \left(\frac{1 + m}{m} \right)^{p_{ij}/2} I_{p_{ij}}(2S_{ij}(m(m + 1))^{0.5}) \quad (4)$$

where S_{ij} is the Huang–Rhys factor for the $|i\rangle \rightarrow |j\rangle$ transition, $I_{p_{ij}}$ is the modified Bessel function of the first kind, and m is the thermal population of the effective vibrational mode

$$m = \frac{1}{\exp\left(\frac{\hbar\omega_{\text{eff}}}{kT}\right) - 1} \quad (5)$$

with k the Boltzman constant and $\hbar\omega_{\text{eff}}$ the energy of the effective accepting mode in the SCC model. p_{ij} is the number of effective phonons required to bridge an energy gap

$$p_{ij} = \frac{E_{ij}}{\hbar\omega_{\text{eff}}} \quad (6)$$

E_{ij} is the adiabatic energy difference between the minima of the potential energy curves of states $|i\rangle$ and $|j\rangle$. For a detailed derivation of these equations, we refer the reader to refs 24 and 25.

We use eqs 2 and 3 to model the temperature dependence of the relative photon counts of the emissions A, B, and D shown in Figure 4. All W_{ij} values are defined as in eq 3 except for W_{20} which is defined as $W_{20} = C_{20}W_{21}$ so as to introduce a “branching ratio” that describes the competition between the nonradiative processes $|2\rangle \rightarrow |1\rangle$ and $|2\rangle \rightarrow |0\rangle$. The fitting parameters are then the three electronic factors C_{32} , C_{21} , and C_{20} as well as $\hbar\omega_{\text{eff}}$.

All the other parameters are deduced from the spectroscopic data and fixed to the values given in Table 3. We include the data obtained for $\text{CsCaI}_3\text{:Tm}^{2+}$ in this comparative study. The radiative rate constants R_i are assumed temperature independent and determined from the lifetimes (Table 2). The high radiative rate constants R_3 of emission D are notable. It might be possible that the ($^3\text{F}_4$, t_{2g}) multiplet is located inside the conduction band and that a mixing of states occurs. States located inside the conduction band can have high radiative decay rate constants.²⁶ The radiative decay rate constant R_3 can be calculated from the oscillator strength f of the first ($^3\text{F}_4$, t_{2g}) absorption band assuming equal degeneracies in the ground and excited state²⁵

$$R = f \frac{n[(n^2 + 2)/3]^2}{\alpha\lambda^2} \quad (7)$$

n is the index of refraction and is estimated to be 1.58, 1.64, and 1.73 for CsCaCl_3 , CsCaBr_3 , and CsCaI_3 , respectively. α is a constant ($1.5 \times 10^4 \text{ s}\cdot\text{m}^{-2}$) and λ is the emission wavelength. We find good agreement of the calculated and measured radiative lifetimes of emission D in all three materials (see Table 2). It is thus unlikely that mixing with the conduction band states of the host affects the luminescent properties of our samples. Luminescence D in $\text{CsCaCl}_3\text{:Tm}^{2+}$ has a nonradiative contribution already at 10 K. In this case, R_3 is given by (at 10 K)

$$R_3 = k_3 - W_{32} \quad (8)$$

k_3 is the measured decay rate constant of emission D at 10 K (Table 2). The branching ratio η_{31} is the experimental photon ratio of bands E/D. The energy gaps E_{ij} are estimated from the absorption and luminescence data. While E_{21} can be accurately determined, there is considerable uncertainty in the value of E_{32} . We use the same value of 2700 cm^{-1} for all three

TABLE 3: Input Parameters from the Experimental Data for the Rate Equation Model Discussed in Section 4.3

	$\text{CsCaCl}_3\text{:Tm}^{2+}$	$\text{CsCaBr}_3\text{:Tm}^{2+}$	$\text{CsCaI}_3\text{:Tm}^{2+}$
E_{32}	2700 s^{-1}	2700 s^{-1}	2700 s^{-1}
E_{21}	3929 s^{-1}	3906 s^{-1}	2995 s^{-1}
S_{32}	0.1	0.1	0.1
S_{21}	2	2	2
R_3	$1\,106\,195 - W_{32}^a \text{ s}^{-1}$	$588\,235 \text{ s}^{-1}$	$954\,000 \text{ s}^{-1}$
R_2	3378 s^{-1}	3096 s^{-1}	2555 s^{-1}
R_1	1996 s^{-1}	1873 s^{-1}	1538 s^{-1}
η_{31}	0.00816	0.00125	0.00123

^a At $T = 10 \text{ K}$.

TABLE 4: Parameters that Are Obtained in the Fit: W_{ij} (calculated from eq 3 using the fitted C_{ij}) and $\hbar\omega_{\text{eff}}$

	$\text{CsCaCl}_3\text{:Tm}^{2+}$	$\text{CsCaBr}_3\text{:Tm}^{2+}$	$\text{CsCaI}_3\text{:Tm}^{2+}$
W_{32} at 10 K	$757\,217 \text{ s}^{-1}$	2532 s^{-1}	$43\,761 \text{ s}^{-1}$
W_{21} at 10 K	0.05 s^{-1}	$3.2 \times 10^{-7} \text{ s}^{-1}$	1.6 s^{-1}
W_{20} at 10 K	0.02 s^{-1}	$1.8 \times 10^{-6} \text{ s}^{-1}$	^a
$\hbar\omega_{\text{eff}}$	106 cm^{-1}	109 cm^{-1}	212 cm^{-1}

^a The process W_{20} is not active in the iodide up to 300 K.

compounds. Similarly, the Huang–Rhys factors S_{21} and S_{32} are set to 2 and 0.1, respectively, for all three compounds. This is a rather crude approximation, since S_{21} is expected to vary across the series. But we have no experimental means of determining this variation, and we want to keep the model as simple as possible. The pump rate constant $\sigma P N_0$ is normalized to 1 s^{-1} . This means that we are in the linear regime and we are ignoring ground-state bleaching.

The integrated photon counts of all three emissions A, B, and D are simultaneously fitted (simple minimization of χ^2 over the parameter space) for a given compound, and the solid lines in Figure 4 represent the best fits. Overall, the model is able to reproduce the data of $\text{CsCaCl}_3\text{:Tm}^{2+}$ and $\text{CsCaBr}_3\text{:Tm}^{2+}$ very well. The deviations are larger for $\text{CsCaI}_3\text{:Tm}^{2+}$. The observed drop of emission A in $\text{CsCaCl}_3\text{:Tm}^{2+}$ above 200 K is the result of energy transfer, see section 5, and thus not within the realm of our photophysical model.

The parameter values obtained in the least-squares fits are listed in Table 4 for the three compounds. A graphical representation of the competition between radiative and non-radiative processes is provided in Figure 9, where the relevant rate constants are logarithmically plotted as a function of temperature for all three systems. It provides insight into the changes that occur along our chemical coordinate.

We are confident that the fits for $\text{CsCaCl}_3\text{:Tm}^{2+}$ and $\text{CsCaBr}_3\text{:Tm}^{2+}$ and the resulting parameter values represent reasonable approximations of the physical reality in these systems. The fitted effective phonon energies for $\text{CsCaCl}_3\text{:Tm}^{2+}$ and $\text{CsCaBr}_3\text{:Tm}^{2+}$ are lower than the highest energy vibrational energies and are comparable with literature data.^{27–29} The effective phonon energy for such nonradiative processes is often lower than the highest energy vibrations.^{27,30} For $\text{CsCaI}_3\text{:Tm}^{2+}$, however, the simple model is a poor approximation of the complex photophysical processes. The best evidence for this is the value of $\hbar\omega_{\text{eff}} = 212 \text{ cm}^{-1}$ obtained for the effective accepting mode. This is higher than any vibrational energy in CsCaI_3 and thus not physical. Evidence for much more complex photophysics in iodide hosts is also provided by the behavior of Tm^{2+} in RbCaI_3 , in which the $4f\text{--}4f$ emission A already dominates at 10 K.¹³ Since our model is extremely simple, there are many possible reasons why it is no longer fully adequate in $\text{CsCaI}_3\text{:Tm}^{2+}$. The necessary caution will therefore be used in the interpretation of the iodide fit in section 5. But it must be

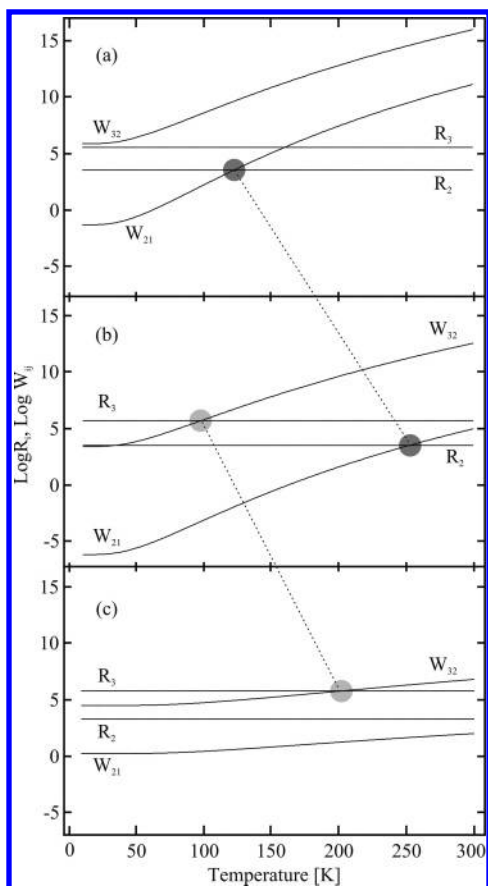


Figure 9. Semilog plot of the radiative R_i and nonradiative W_{ij} rate constants as a function of temperature for Tm^{2+} doped CsCaCl_3 (a), CsCaBr_3 (b), and CsCaI_3 (c). The radiative rate constants R_i are given in Table 3. The nonradiative rate constants W_{ij} are calculated from eq 3 using the parameter values in Tables 3 and 4. The crossover points of W_{32} with R_3 and W_{21} with R_2 are highlighted and connected with dashed lines for better illustration of the influence of the chemical variable on the photophysics of Tm^{2+} .

noted that an analysis of the type provided in Figure 4 with the parameters in Tables 3 and 4 is extremely ambitious and has not been reported so far. Fits of the temperature dependence of emission intensities or lifetimes are usually done for just one transition in one compound.^{27–31} We extend this by including three competing transitions in each of three related compounds, and we do this without adjusting the model. We thus gain considerably more insight into the photophysics and their dependence on the chemical variable in these systems. But we do reach the limit of applicability of the model.

5. Discussion

Each of the five emissions A–E will be discussed separately, with the main emphasis on its variation with temperature for a given compound and its variation along the series of Tm^{2+} doped halides.

Emission D is the highest energy emission in the chloride and bromide. In the iodide, we observe a weak emission below 200 K, which lies at even higher energy. This is discussed in ref 13. In all three compounds, emission D appears bright green to the eye. It is a broad 5d–4f emission band and has its origin in the lowest states of the ($^3\text{F}_4$, t_{g}) multiplet. With the exception of 4f–4f emissions in lanthanides and actinides, Kasha’s rule is a guiding principle for light-emitting materials.³² It states that, if at all, spontaneous emission occurs from the lowest-energy excited state. Our emission D is an exception to this rule, and

to our knowledge, emission from higher than the lowest-energy “spin-allowed” and “spin-forbidden” 4f–5d states has not been reported in lanthanide systems.¹²

On the basis of Figure 9, we can understand how this exceptional behavior comes about. First, we note that emission D has the highest radiative rate constant (R_3) of all the observed emissions. R_3 is the dominant relaxation path in the iodide up to 220 K, in the bromide up to 100 K. At these temperatures, the crossing of W_{32} with R_3 occurs in the two samples and thus nonradiative relaxation to ($^3\text{H}_6$, t_{g}) becomes the dominant relaxation process at elevated temperatures. These crossover points are highlighted and connected with a dashed line in Figure 9. In the chloride, R_3 has a strong competition already at 10 K from the nonradiative W_{32} , and above 50 K, R_3 loses out completely; see also data in Figure 4. The comparison of the three samples shows the strong dependence of W_{32} on the chemistry. W_{32} decreases by 2 orders of magnitude at 10 K in the bromide compared to the chloride, but for $\text{CsCaI}_3\text{:Tm}^{2+}$, the values lie between the two others. A decrease of W_{32} (10 K) along the halide series is expected on the basis of decreasing phonon energies. The observed increase in the iodide clearly shows the limits of the model. The evolution of W_{32} with temperature is similar in the chloride and bromide, whereas in the iodide, the increase with temperature is much less steep. The chemical variation thus affects not only the 10 K value of W_{32} but also its temperature dependence, with a significant difference in the iodide.

Emission E has the same temperature dependence and originates from the same state as D, but the final state is $^2\text{F}_{5/2}$ instead of the ground state. It is extremely weak, with D/E photon ratios of 123:1, 800:1, and 806:1 in the chloride, bromide, and iodide, respectively. We ascribe this extreme branching ratio to a selection rule $\Delta J = 1$.³³ The lowest-energy component of ($^3\text{F}_4$, t_{g}) has, according to Hund’s rule, a $J = 9/2$ value, if we only consider the spin angular momentum of the 5d electron. Thus, a transition to $^2\text{F}_{7/2}$ is allowed, whereas $^2\text{F}_{5/2}$ is not accessible in this rough approximation.

Emission B is a broad 5d–4f band in the near-IR around $12\,000\text{ cm}^{-1}$. It is assigned to a transition from the lowest-energy ($^3\text{H}_6$, t_{g}) $S = 3/2$ to $^2\text{F}_{7/2}$. It is the dominant feature in the emission spectrum of the chloride up to 120 K, of the bromide between 100 and 250 K, and of the iodide above 220 K; see also Figures 3 and 4. ($^3\text{H}_6$, t_{g}) $S = 3/2$ is being populated by multiphonon relaxation (W_{32}) from the higher ($^3\text{F}_4$, t_{g}) metastable state. Since the decrease of emission D with increasing temperature is also determined by W_{32} , we can immediately understand that the observed rise with the temperature of B is correlated with the decline of D, nicely seen in Figure 4 for all three samples. The lifetime of emission B is constant up to 70 and 160 K in $\text{CsCaCl}_3\text{:Tm}^{2+}$ and $\text{CsCaBr}_3\text{:Tm}^{2+}$, respectively (see Figure 5), which proves the radiative nature of the decay up to these temperatures. Above 120 K in the chloride and 250 K in the bromide, emission B is taken over by emission A. Their correlated rise and decline is again nicely observed in Figure 4. The nonradiative relaxation process from ($^3\text{H}_6$, t_{g}) $S = 3/2$ to $^2\text{F}_{5/2}$ (W_{21}) is responsible for this, see the crossing of W_{21} with R_2 at 120 and 250 K in the chloride and bromide, respectively, in Figure 9. This onset of nonradiative relaxation is also confirmed by the simultaneous decrease of the respective lifetimes in Figure 5. In the iodide, the W_{21} process is not competitive up to room temperature, that is, we observe no crossing point of W_{21} with R_2 .

Emission C is a weak emission only observed in the bromide and iodide that originates in a higher excited state within the

($^3\text{H}_6, t_{\text{ig}}$) multiplet. We assign it to the ($^3\text{H}_6, t_{\text{ig}}$) $S = 1/2 \rightarrow ^2\text{F}_{7/2}$ transition. This is a formally “spin-allowed” transition with a high oscillator strength. The energy difference between the lowest level of ($^3\text{H}_6, t_{\text{ig}}$) $S = 1/2$ and the highest level of ($^3\text{H}_6, t_{\text{ig}}$) $S = 3/2$ is difficult to estimate from the absorption and luminescence spectra: A range of 600–1200 cm^{-1} is compatible with the data. This is a very small gap, and in all compounds studied here, relaxation by multiphonon processes is active down to the lowest temperatures. In the chloride, multiphonon relaxation is too efficient for C to be observed. In the bromide, the intensity of C compared to B is small, whereas in the iodide, C has gained considerable intensity. The observation of emission C in the bromide and iodide is surprising considering the small energy gaps involved. In Ce^{3+} doped compounds, energy gaps of up to several thousand cm^{-1} are observed between the states deriving from the ($4f^05d^1$) electron configuration.^{34,35} Generally, only emission from the lowest state is observed. Multiphonon relaxation among states of the same spin multiplicity appears to be efficient. In contrast, the multiphonon relaxation process from ($^3\text{H}_6, t_{\text{ig}}$) $S = 1/2$ to $S = 3/2$ requires a reorientation of the spin, which slows it down. This is considered a key to the observation of emission from the low-spin state.³⁶ Among the lanthanides having a more than half-filled 4f shell, “spin-forbidden” and “spin-allowed” emissions have been reported for Yb^{2+} ,¹² Er^{3+} , and Tm^{3+} doped compounds.^{36,37} The ratio of “spin-forbidden” and “spin-allowed” emission was found to depend on the host and the temperature.

Emission A ($^2\text{F}_{5/2} \rightarrow ^2\text{F}_{7/2}$) is the strongest emission at 300 K in the chloride and bromide. The emitting state $^2\text{F}_{5/2}$ is populated from ($^3\text{H}_6, t_{\text{ig}}$) $S = 3/2$ by the multiphonon relaxation process with rate constant W_{21} . A takes over from B as the most intense emission at about 120 and 250 K, respectively; in the two lattices, see Figure 4 and the crossing points of R_2 with W_{21} in Figure 9. In the iodide, this crossing is not reached below 300 K, because W_{21} is not competitive. It is interesting to note that a very small A emission of the order of 0.1% is observed even at 10 K in all three samples; see Table 1. In the bromide, the $^2\text{F}_{5/2}$ population occurs purely radiatively by process E, whereas in chloride and iodide there is an additional nonradiative contribution to the $^2\text{F}_{5/2}$ feeding. In $\text{CsCaCl}_3\text{:Tm}^{2+}$, the intensity of emission A decreases above 200 K. This is not due to multiphonon relaxation to the ground state, for which the energy gap of 8800 cm^{-1} is too large. We ascribe it nonradiative losses by energy migration to unidentified killer traps.

6. Conclusions and Outlook

The temperature-dependent study of the emission properties of Tm^{2+} doped into a series of isostructural halide lattices provides insights into the photophysics of this ion. The interplay and the competition of the various radiative and nonradiative relaxation processes are elucidated, and the rate constants of the relevant processes are quantified. The observation and characterization of up to five different types of light emission from a given compound, which is without precedent, provide the basis for such a detailed analysis. It turns out that the chemical variation along the series of CsCaCl_3 , CsCaBr_3 , and CsCaI_3 host lattices and its significant consequences on the light-emission behavior are essential for the relatively detailed picture obtained. The pronounced temperature dependence of the nonradiative processes is an important factor, which we are reproducing with an approximate model in the present paper, whereas the radiative decay constants are essentially temperature independent. In the iodide, we reach the limit of the applicability of the simple model. But it does allow a discussion of the relevant processes and their temperature dependence.

The choice of Tm^{2+} as the active ion turns out to be fortunate for both chemical and physical reasons. It is possible to stabilize the divalent Tm in all the halides (chloride, bromide, and iodide). Physically, a big advantage of the ($4f^{13}$) electron configuration of Tm^{2+} lies in the fact that $^2\text{F}_{5/2}$ is the only 4f–4f excited state, and above 9000 cm^{-1} , the properties of the states arising from the ($4f^{12}5d^1$) configuration can be probed without any interference from the ($4f^{13}$) configuration. The observation of emissions from higher excited 4f–5d states is facilitated by the fact that we are dealing with divalent host lattices with heavy anions. A practical advantage of the systems studied here is the energy range of the emissions studies, from the near-IR to the green, which is experimentally more easily accessible than the vacuum UV, where the 5d–4f emissions of the trivalent lanthanides are often found.

Let us finally briefly compare the light-emission properties reported and analyzed here in chloride, bromide, and iodide lattices with literature studies of Tm^{2+} doped fluorides. All these studies deal with the 4f–4f emission in the near-IR, and we found no report of 5d–4f emission in a fluoride, even at cryogenic temperatures. This may simply be a reflection of a very efficient ($^3\text{H}_6, t_{\text{ig}}$) $S = 3/2$ to $^2\text{F}_{5/2}$ nonradiative relaxation rate constant W_{21} . However, there are chemical considerations that have to be taken into account. Tm^{2+} is harder to stabilize in a fluoride than in the heavier halides. As a consequence, Tm^{3+} is invariably present in Tm^{2+} doped fluorides, and this might quench the emission B of Tm^{2+} by energy transfer. We have found some preliminary evidence of emission B in a $\text{CaF}_2\text{:Tm}^{2+}$ sample, in which Tm^{2+} was chemically incorporated and not created by irradiation as in some of the other investigations.

Acknowledgment. The authors thank K. W. Krämer and D. Biner for their assistance concerning crystal synthesis. P. Gerner and A. Sieber are acknowledged for valuable discussions. The Swiss National Science Foundation is gratefully acknowledged for financial support.

References and Notes

- Rubio, J. *J. Phys. Chem. Solids* **1991**, *52*, 101.
- Meyer, G. *Chem. Rev.* **1988**, *88*, 93.
- McClure, D. S.; Kiss, Z. J. *J. Chem. Phys.* **1963**, *39*, 3251.
- Kiss, Z. J. *Phys. Rev.* **1962**, *127*, 718.
- Loh, E. *Phys. Rev.* **1968**, *175*, 533.
- Duncan, R. C.; Kiss, Z. J. *J. Appl. Phys. Lett.* **1963**, *3*, 23.
- Duncan, R. C. *IEEE J. Quantum Electron.* **1966**, *2*, R52.
- Schipper, W. J.; Meijerink, A.; Blasse, G. *J. Lumin.* **1994**, *62*, 55.
- Wenger, O. S.; Wickleder, C.; Krämer, K.; Güdel, H. U. *J. Lumin.* **2001**, *94–95*, 101.
- Wickleder, C. *J. Alloys Compd.* **2000**, *300–301*, 193.
- Grimm, J.; Güdel, H. U. *Chem. Phys. Lett.* **2005**, *404*, 40.
- Dorenbos, P. *J. Phys.: Condens. Matter* **2003**, *15*, 575.
- Beurer, E.; Grimm, J.; Güdel, H. U. To be submitted for publication.
- Meyer, G. *Adv. Synth. React. Solids* **1994**, *2*, 1.
- Seifert, H.-J.; Langenbach, U. *Z. Anorg. Allg. Chem.* **1969**, *368*, 36.
- Seifert, H.-J.; Haberhauer, D. *Z. Anorg. Allg. Chem.* **1982**, *491*, 301.
- Vaills, Y.; Buzaré, J. Y.; Gibaud, A.; Launay, C. *Solid State Comm.* **1986**, *60*, 139.
- Lucas, M. C. M.; Rodriguez, F.; Prieto, C.; Verdager, M.; Güdel, H. U. *J. Phys. Chem. Solids* **1995**, *56*, 995.
- Schilling, G.; Meyer, G. *Z. Anorg. Allg. Chem.* **1996**, *622*, 759.
- Hüfner, S. *Optical Spectra of Transparent Rare Earth Compounds*; Academic Press: New York, 1978.
- Dorenbos, P. *J. Phys.: Condens. Matter* **2003**, *15*, 6249.
- Richardson, F. S.; Reid, M. F.; Dallara, J. J.; Smith, R. D. *J. Chem. Phys.* **1985**, *83*, 3813.
- Struck, C. W.; Fonger, W. H. *J. Lumin.* **1975**, *10*, 1.
- Donnelly, C. J.; Imbusch, G. F. In *Advances in Nonradiative Processes in Solids*; di Bartolo, B., Ed.; NATO ASI Series; Plenum Press: New York, 1991; pp 175–195.
- Henderson, B.; Imbusch, G. F. *Optical Spectroscopy of Inorganic Solids*; Oxford University Press: New York, 1989.

- (26) Dorenbos, P. *J. Phys.: Condens. Matter* **2003**, *15*, 2645.
(27) Reber, C.; Güdel, H. U. *J. Lumin.* **1988**, *42*, 1.
(28) May, P. S.; Güdel, H. U. *J. Lumin.* **1990**, *46*, 277.
(29) Gamelin, D. R.; Güdel, H. U. *J. Phys. Chem. B* **2000**, *104*, 10222.
(30) Sturge, M. D. *Phys. Rev. B* **1973**, *8*, 6.
(31) Donegan, J. F.; Bergin, J. F.; Glynn, T. J.; Imbusch, G. F. *J. Lumin.* **1986**, *35*, 57.
(32) Kasha, M. *Discuss. Faraday Soc.* **1950**, *9*, 14.
(33) Peijzel, P. S.; Vergeer, P.; Meijerink, A.; Reid, M. F.; Boatner, L. A.; Burdick, G. W. *Phys. Rev. B* **2005**, *71*, 045116.
(34) Dorenbos, P. *Phys. Rev. B* **2000**, *62*, 15640.
(35) Dorenbos, P. *Phys. Rev. B* **2000**, *62*, 15650.
(36) Wegh, R. T.; Meijerink, A. *Phys. Rev. B* **1999**, *60*, 10820.
(37) van Pieterse, L.; Wegh, R. T.; Meijerink, A.; Reid, M. F. *J. Chem. Phys.* **2001**, *115*, 9382.